JMEPEG (2021) 30:7314–7327
https://doi.org/10.1007/s11665-021-05958-z

1059-9495/$19.00

Improvement of Corrosion and Wear Resistance of Ni-W Coatings by Embedding Graphene Oxide Modified by Nano-Al_2O_3

Zhang Guosong, Cui Hongzhi, Song Xiaojie, Tian Shuichang, and Su Chunjian

Submitted: 31 March 2020 / Revised: 5 April 2021 / Accepted: 15 May 2021 / Published online: 14 June 2021

Graphene oxide (GO) easily aggregates due to the cross-linking between divalent cations in the plating baths, and the presence of reduced GO in metal coatings promotes corrosion. This paper aims to improve the corrosion and wear resistance of Ni-W coatings by embedding graphene oxide modified with nano-Al_2O_3 nanoparticles (Al_2O_3@GO). Carboxylic acid groups were removed to eliminate cross-linking with divalent cations. Moreover, the increased number of hydroxyl groups ensured that Al_2O_3@GO was highly dispersed in the plating bath. Then, Ni-W-Al_2O_3@GO coatings were fabricated by pulse electrodeposition with different Al_2O_3@GO concentrations in the plating solution. The grain refinement, low number of defects, and low conductivity (1.31 Sm^{-1}) of the reduced Al_2O_3@GO in the coating gave it anti-corrosion properties. The coating with 1 g L^{-1} of GO addition (*Icorr = 0.195* µA) displayed better corrosion and wear resistance properties than Ni-W coating (*Icorr = 6.66* µA), Ni-W-GO coating (*Icorr = 0.706* µA), and other Ni-W-Al_2O_3@GO coatings. The uniform distribution of Al_2O_3@GO in the coatings allowed it to serve as a physical barrier which eliminated electron pathways and prevented the infiltration of corrosive media. Moreover, the self-lubrication and similar "rolling" of Al_2O_3@GO increased the wear resistance of the coatings.

Keywords Al_2O_3 nanoparticles, graphene oxide, Ni-W coating, wear and corrosion resistance

1. Introduction

Nickel-tungsten (Ni-W) alloy coatings are used in many aggressive environments as environment-friendly substitutes for hard chromium films. Ni-W coatings have high hardness, high thermal stability, and anti-wear and anti-corrosion properties (Ref 1-4) which are influenced by the structure of the coating and W contents. The addition of W to Ni alloys decreases the crystallite size because of the preferred crystal plane lies along the (111) plane instead of the (200) (Ref 5). Tungsten also increases the hardness due to the solid solution strengthening and grain refinement (Ref 6, 7) and can also increase the corrosion resistance of Ni composite coatings, but this trend is not consistent (Ref 5). It has been shown that the anti-corrosion property of Ni-W alloys initially increases upon the gradual refinement of the nanocrystalline grains with increasing W content. However, the anti-corrosion property begins to decrease due to an increased volume of the intercrystalline region of the triple junction accompanied by a particularly small crystallite size (Ref 8). Moreover, the excess W generates residual tensile stress in the composite coating, which simultaneously decreases the solution stability and cathode current efficiency (Ref 9). Nano- and microsized inorganic inert particles—such as Al_2O_3 (Ref 10-12), TiO_2 (Ref 13), SiO_2 (Ref 14), ZrO_2 (Ref 15), Si_3N_4 (Ref 16), SiC (Ref 17), WC (Ref 18), diamond (Ref 19), CeO_2 (Ref 20), MWCNTs (Ref 21), and BN(h) nanoparticles (Ref 22)—have been shown to enhance the hardness of coatings and decrease the residual tensile stress. Additionally, their characteristics and content in coatings affect the performance of composite coatings.

Graphene, single-layer 2D sp2-hybridized carbon (Ref 23), shows remarkable physical and chemical properties (Ref 24-27) and has been shown to improve the mechanical properties, corrosion resistance, and anti-friction properties of Ni alloys (Ref 28-30). Previous studies have reported that Ni composite coatings embedded with graphene sheets can be prepared via electrodeposition. Unfortunately, maintaining a uniform graphene distribution in the plating solution is difficult due to its hydrophobic surface and chemical stability (Ref 31). Graphene oxide (GO), which contains oxygenous functional groups on its surface, can form well-dispersed aqueous colloids (Ref 32, 33). Moreover, GO sheets are compatible with metal matrixes due to the presence of oxygen groups on its surface. Fan et al. (Ref 34) used pulse electrodeposition to prepare Ni-W-GO sheet composite coatings with increased corrosion potentials due to the shielding of micropores by GO. The hardness and wear resistance of a Ni-W-GO composite coating obtained by direct current co-deposition were improved by the addition of GO sheets (Ref 35).

Zhang Guosong, College of Mechanical and Electronic Engineering, Shandong University of Science and Technology, Qingdao 266590, China; and Shandong Province Key Laboratory of Mine Mechanical Engineering, Shandong University of Science and Technology, Qingdao 266590, China; **Cui Hongzhi, Song Xiaojie,** and **Tian Shuichang**, School of Materials Science and Engineering, Shandong University of Science and Technology, Qingdao 266590, China; **Su Chunjian**, College of Mechanical and Electronic Engineering, Shandong University of Science and Technology, Qingdao 266590, China. Contact e-mails: zhguosong@sdust.edu.cn and cuihongzhi1965@163.com.

Three primary aspects affect the co-deposition of Ni-W-GO sheets. Firstly, due to cross-linking between metals and the carboxylic acid groups of GO sheets (Ref 36), GO sheets are prone to aggregation, which leads to an uncontrollable precipitation in the plating bath that contain divalent cations. Secondly, GO sheets in the plating bath are constantly reduced during electrodeposition (Ref 37), and the reduced GO sheets (RGO) easily aggregate. Lastly, RGO can be deposited into coatings, which promotes the corrosion by changing the electron transfer behavior between the metal, coating, and electrolyte interface (Ref 38). Various methods have been developed to overcome these limitations. For example, GO has been dispersed in epoxy coatings by mutual surface modification with silane and titanium dioxide (Ref 39), oxide-alumina (Ref 40), and silica (Ref 41, 42). This improved the anti-corrosion properties of composite epoxy coatings due to the uniform and stable dispersion of decorated GO sheets. PVB coatings embedded with RGO sheets modified by low-conductivity pernigraniline displayed outstanding anti-corrosion behavior. The SAT-G (a novel aniline trimer (AT) functionalized graphene sheets) (Ref 43) and super-hydrophobic polyhedral oligomeric silsesquioxane functionalized graphene (Ref 44) were added into epoxy matrix. As a result, the functionalization could effectively increase the dispersion of graphene in epoxy matrix, and the anti-corrosion and wear-resistant of epoxy coating were improved. Then, Ye et al. (Ref 45) prepared CDs (functionalized carbondots)-modified graphene/epoxy (CDs-G/EP) coatings, and the dispersion and interface compatibility of graphene were greatly enhanced by CDs, and the coating had a superior protective property on steel. In addition to the longer diffusion pathway of corrosive media into the matrix, the anti-corrosion property was attributed to the excellent dispersion of RGO sheets in the coating (Ref 46). RGO-PVA composite films exhibited excellent corrosion resistance and anti-wear properties on a Mg alloy surface by preventing contact between graphene sheets (Ref 47).

These previous results show that the agglomeration of GO sheets can be minimized by surface modification. Thus, the aim of this work was to prevent the agglomeration of GO in the Ni-W plating bath and reduce the conductivity of RGO in the coatings by modifying the surface of GO sheets. Here, GO sheets were modified with Al_2O_3 nanoparticles (Al_2O_3@GO), and the characteristics of Al_2O_3@GO and reduced Al_2O_3@GO were studied. Then Ni-W-Al_2O_3@GO composite coatings were fabricated by pulse electrodeposition with different concentrations of Al_2O_3@GO sheets in the plating solution. Finally, the corrosion resistance and anti-friction performances of the composite coatings were investigated systematically.

2. Experimental

2.1 Materials

C45 steel samples were used as the substrate material (quenching and tempering treatment, 15 mm X 15 mm X 5 mm) and were mechanically polished (Ra $\leq$ 1 μm).

2.2 Synthesis of GO@Al_2O_3 Hybrids

First, αAl_2O_3 nanoparticles ($<$ 30 nm, SEM images and XRD pattern are shown in Fig. 1) were functionalized. Al_2O_3 nanoparticles (1 g) and 8-aminopyrene-1,3,6-trisulfonic acid trisodium salt (APTS, 20 g) were dissolved in anhydrous ethanol (500 mL) and stirred for 4 h at 78 °C. The reaction mixture was then diluted by the slow addition of DI water (40 g), followed by filtration. Functionalized Al_2O_3 nanoparticles (f-Al_2O_3) were washed several times with anhydrous ethanol and DI water and dried for 24 h at 60 °C under vacuum environment.

In order to synthesize Al_2O_3@GO hybrids, a homogeneous suspension was created by dissolving 0.1 g functionalized Al_2O_3 in 250 mL *N*, *N*-dimethylformamide (DMF) via ultrasonication for 2 h. Then, 0.5 g GOs (Nanjing XFNANO Materials Tech Co., Ltd) were added into the suspension with ultrasonication for 120 min. The obtained solution was refluxed with continuous stirring at 105 °C for 5 h. The obtained GO@Al_2O_3 hybrids were filtered, washed, and then dried for 24 h at 60 °C under vacuum (Ref 40).

2.3 Preparation of Ni-W-GO, Ni-W-Al_2O_3@GO Composite Coatings

The composition of the plating bath and the operational conditions are listed in Table 1. The pH was adjusted with sulfuric acid and ammonium hydroxide. Al_2O_3@GO or GO sheets firstly were dispersed in DI water by stirring at 400 rpm for 24 h and then in an ultrasonic bath for 60 min. The plating

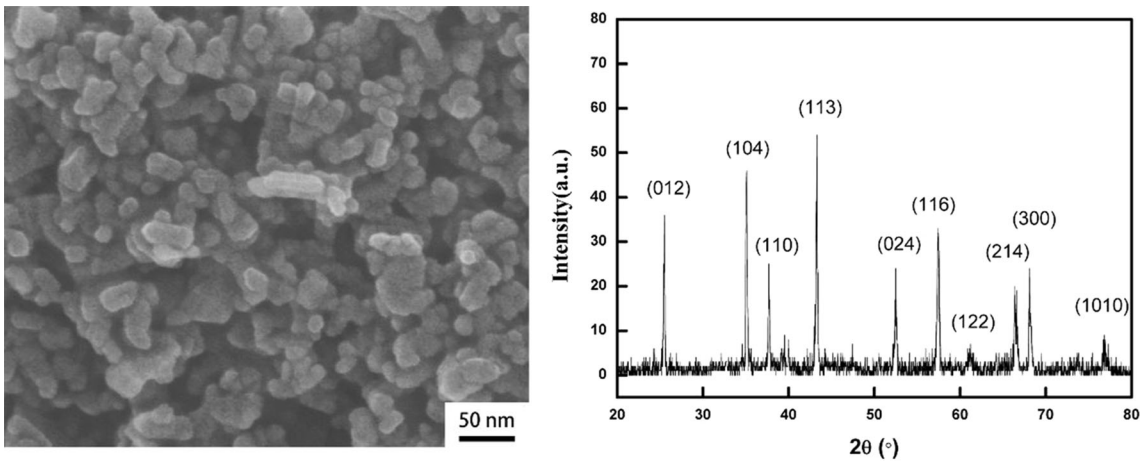

Fig. 1. SEM images and XRD pattern of the Al_2O_3 nanoparticles

bath was stirred at 200 rpm constant speed during electrodeposition process.

2.4 Characterization

The synthesized materials were characterized by electron probe microanalyzer (EPMA, JEOL JXA-8230, Japan; acceleration voltage: 15 kV), field emission scanning electron microscopy in the secondary electron mode at an acceleration voltage of 15 kV (FESEM, FEI Nova Nanosem 450, USA), transmission electron microscopy (TEM Philips CM200) working at 200 kV and equipped with a super-twin objective lens, Raman spectroscopy (Bruker Senterra R200-L; laser wavelength: 532 nm; power: 20 mW), x-ray diffraction (XRD, Rigaku, D/Max2500PC, Japan; Cu kα radiation source; λ = 0.15405 nm; 40 kV; 40 mA) by scanning in the range of 20° to 80°, Fourier-transform infrared spectroscopy (FTIR, Nicolet 380, USA) with a 4 cm^{-1} resolution over a wavenumber range of 400-4000 cm^{-1}, and x-ray photoelectron spectroscopy (XPS, Thermo ESCALAB 250XI, USA) with a magnesium anode producing Al kα x-rays. GO and Al_2O_3@GO were reduced by hydrazine hydrate, and their conductivities were determined by a four-point probes (ST2263, SuZhou).

Table 1 Bath composition and operating conditions

Composition and conditions	
$NiSO_4{\cdot}6H_2O$	20 g L^{-1}
$Na_2WO_4{\cdot}2H_2O$	45 g L^{-1}
$NiCl_2$	5 g L^{-1}
NaBr	15 g L^{-1}
Na_3Cit	60 g L^{-1}
NH_4Cl	27 g L^{-1}
Sodium dodecyl sulfate	0.5 g L^{-1}
Saccharin sodium	2 g L^{-1}
Al_2O_3@GO, GO 1 g L^{-1}	0.5, 1, 2, 3 g L^{-1}
pH	7
Temperature	50 °C
Average current density	8 A dm^{-2}
Duty cycle	0.2
Frequency	400 Hz
Time	40 min

The anti-corrosion properties of coatings were investigated using electrochemical measurements (Gamry Reference 3000 potentiostat) in 3.5% NaCl solution at room temperature. Electrochemical impedancespectroscopy (EIS) was carried out in the range of 10^{-2}-10^5 Hz with a 10 mV AC amplitude. Potentiodynamic polarization measurements were conducted by scanning from −500 mVSCE to 500 mVSCE at a rate of 1mV s^{-1}. The electrical conductivities were measured using a four-point probe setup.

The tribological properties of coatings were evaluated using a reciprocating ball-on-plate universal tester at room temperature (Model: MFT-5000, Brand: RTEC), with a reciprocating frequency of 1 Hz, a sliding distance of 10 mm, and loads of 1 N and 10 N. A zirconia wear-resistant ceramic ball with a diameter of 9.525 mm was used as the counter-body.

3. Results and Discussion

3.1 Structure and Morphology of Al_2O_3@GO Hybrids

3.1.1 SEM and TEM Images. Figure 2 shows the morphologies of GO and Al_2O_3@GO hybrids. The wavy or "wrinkled" nature of the GO is shown in Fig. 2(a). As shown in Fig. 2(b), the spherical Al_2O_3 nanoparticles were anchored directly on the surface of GO sheets, and the creased and wrinkled morphology of GO was maintained. This indicates that the layered structure of the GO sheets was not destroyed during Al_2O_3@GO fabrication.

The structure and morphology of Al_2O_3@GO were further investigated using TEM and HRTEM. HAADF images (Fig. 3a), TEM images (Fig. 3b), and HRTEM images (Fig. 3d) showed that the Al_2O_3 particles were tightly coated on the surface of the GO sheets. Figure 3c shows the EDS elemental mapping corresponding to Fig. 3(a), which indicates that the slices were GO, and the particles were Al_2O_3.

3.1.2 Raman Analysis. The Raman spectra of GO and Al_2O_3@GO hybrids are shown in Fig. 4. Two peaks were present for GO, i.e., the D-band at 1351 cm^{-1} and the G-band at 1606 cm^{-1}. After modification by Al_2O_3 nanoparticles, the G-band was broadened and shifted to 1617 cm^{-1}, which indicates that the Al_2O_3@GO hybrid layers were more exfoliation (Ref 48). Furthermore, the I_D/I_G ratio value (where I_D and I_G are the D-band and G-band Raman intensities,

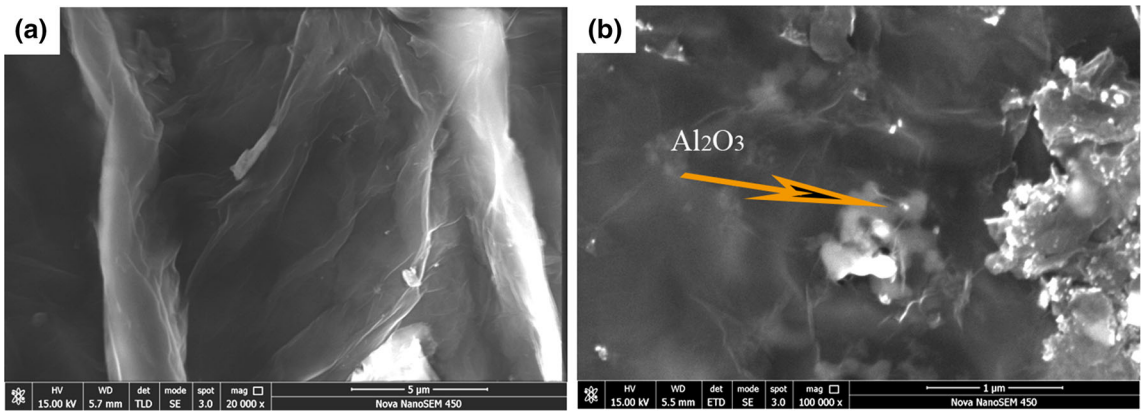

Fig. 2. FESEM micrographs of (a) GO and (b) Al_2O_3@GO

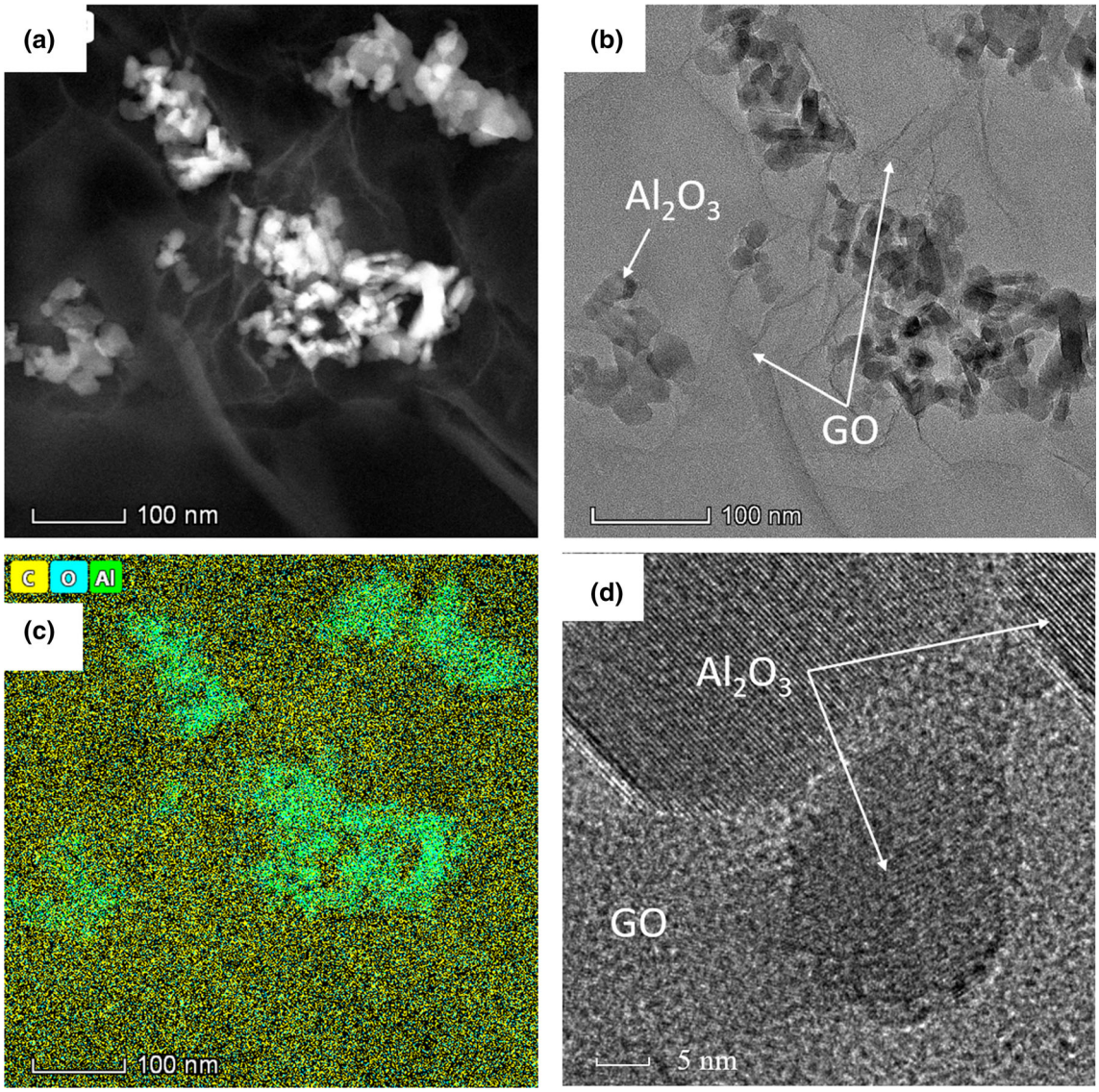

Fig. 3. HAADF (a), TEM (b), HRTEM (d) images and EDS elemental mapping (c) of Al_2O_3@GO

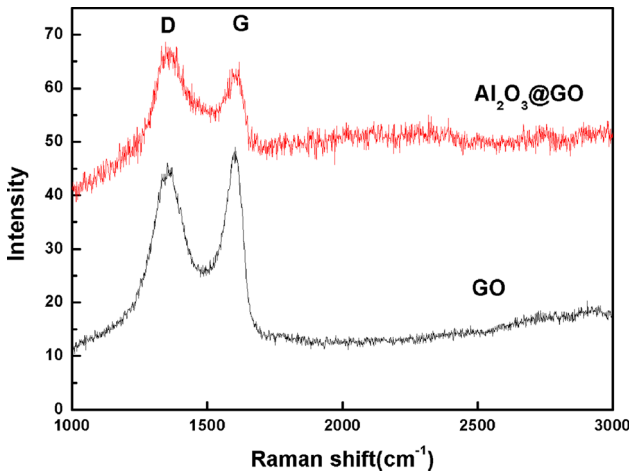

Fig. 4. Raman spectra of GO and Al_2O_3@GO

respectively) increased to ~ 1.07 for the Al_2O_3@GO hybrids, compared with that of GO of 0.89. This indicates the destruction of symmetry and the distortion of bonds, possibly due to a reduction in the size of the in-plane sp2 domains, which was enhanced by modification with Al_2O_3 nanoparticles (Ref 49).

3.1.3 FTIR Spectra. The FTIR spectra of GO sheets and Al_2O_3@GO are shown in Fig. 5(a). There are various peaks in the GO spectrum, including -OH (3360, and 1381 cm^{-1}), -CH_2 (2968 cm^{-1}), C=O (1701 cm^{-1}), C=C (1594 cm^{-1}), and C-O (1381 cm^{-1}) groups on the surface of GO. In the FTIR spectrum of Al_2O_3@GO, the CH_2 and C=O peaks disappear, and the intensities of the -OH peaks (3430 cm^{-1} and 1381 cm^{-1}) were enhanced. New peaks also appeared at 2817, 826, and 626 cm^{-1} which belonged to C-H bending, N-H rocking, and Si-O-Al stretching. The disappearance of C=O and CH_2 and the appearance of N-H on the surface of Al_2O_3@GO revealed that chemical reactions occurred between the carboxyl groups of GO and the NH_2 groups of f-Al_2O_3. Furthermore, the broad absorption band corresponding to the Al-O-Al bond of

Al_2O_3 appeared from 500 to 1000 cm^{-1}, which confirmed the interaction between nano-Al_2O_3 and the GO sheets (Ref 40). The increased intensity of the -OH peaks in the Al_2O_3@GO spectrum was attributed to f-Al_2O_3 due to the presence of hydroxyl groups on the surface (Ref 50).

The FTIR spectra of RGO and R@GO (Fig. 5b) show that the GO peaks completely vanished, showing that oxygen functionalities were removed and GO was reduced. The FTIR spectrum of R@GO shows that the hydroxyl (3430 cm^{-1}), C-H bending, N-H rocking, and Si-O-Al stretching still remained. Retaining the oxygen functionalities on the surface of the R@GO sheets ensured that Al_2O_3@GO remained hydrophilicity and well dispersed during the plating process.

3.1.4 XPS Analysis. To confirm changes in the functional groups between the GO and Al_2O_3@GO, their C 1*s* XPS spectra were obtained (Fig. 6). Figure 6(a) shows the C 1*s* XPS spectrum of the GO sheets. The presence of four carbon peaks indicated considerable oxidation: non-oxygenated ring C, C in C-O bonds, carbonyl C, and the carboxylate C (O-C=O). The C 1s XPS spectrum of Al_2O_3@GO is shown in Fig. 6(b) and contained the same four carbon functional groups as GO. More importantly, the peak intensity of C(=O)-O nearly disappeared, which indicates that carboxyl groups in GO were removed after modification with Al_2O_3. The FTIR and XPS results indicate that most carboxyl groups were removed from the GO surface, and more hydroxyl groups appeared on the surface of Al_2O_3@GO during modification by Al_2O_3. The structure of Al_2O_3@GO is illustrated in Fig. 7.

3.2 Characterization of Composite Coatings

3.2.1 XRD Analysis. XRD was applied to determine the phase composition and microstructure of the fabricated coatings. Figure 8 shows the XRD pattern comparison of Ni-W, Ni-W-GO (GO: 2 g L^{-1} concentration), and Ni-W-Al_2O_3@GO composite coatings which show that Ni-W coatings were a Ni-based solid solution with an fcc structure. All patterns exhibited a prominent peak at 44.31° corresponding to the (111) crystal plane of nickel, and peaks at 52.56° and 77.9° corresponding to the (200) and (220) crystal planes, respectively (JCPDS Card No. 65-4828). The peaks at (200) and (220) were weakened due to doping by GO and Al_2O_3@GO, which indicated that GO and Al_2O_3@GO were introduced into the coatings and affected the preferred orientation of Ni. The average grain size of the coatings was calculated by the Debye–Scherrer equation

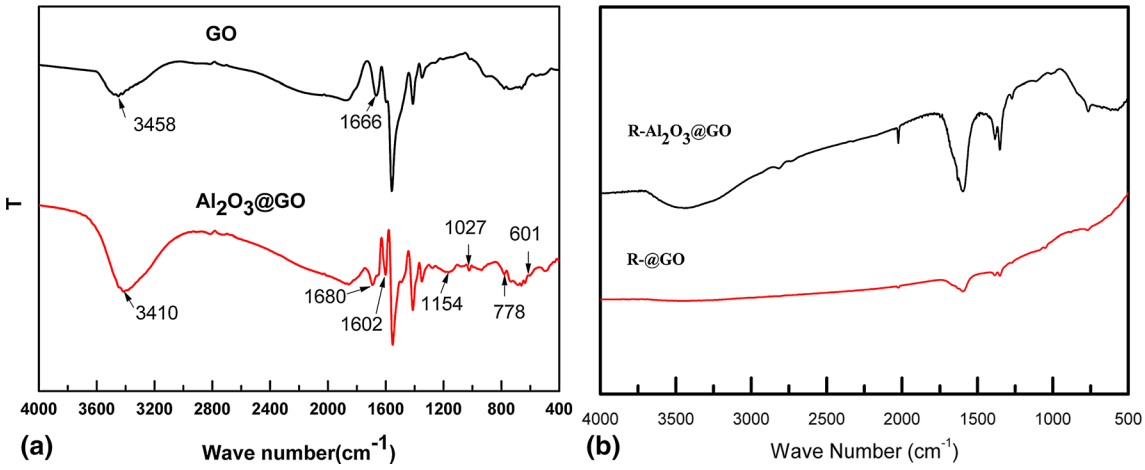

Fig. 5. The FTIR spectra of (a) GO, Al_2O_3@GO; (b) RGO, R@GO

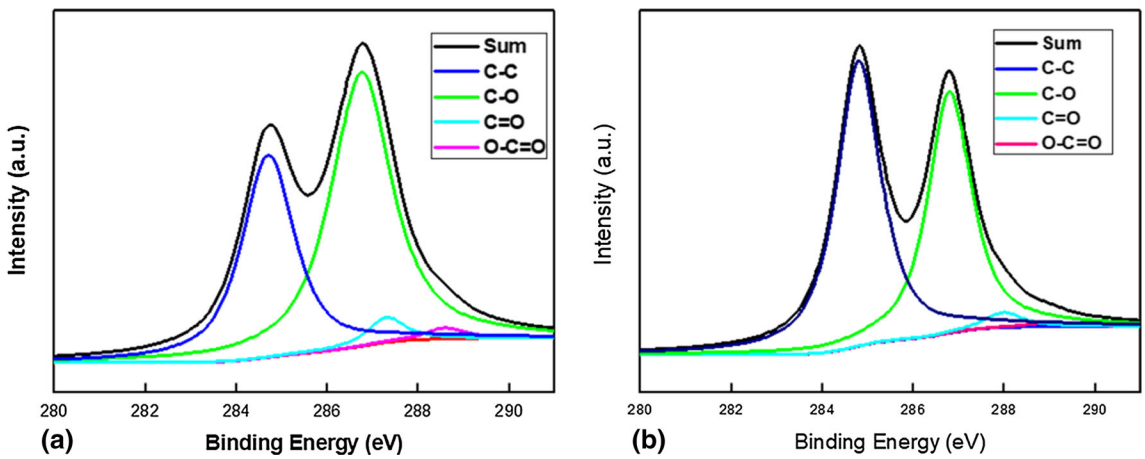

Fig. 6. The C1s XPS spectra of: (a) GO, (b) Al_2O_3@GO

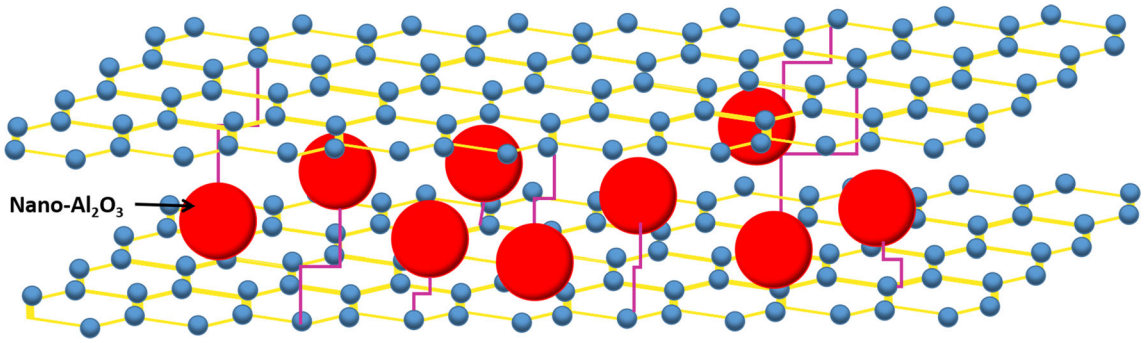

Fig. 7. Illustration of Al_2O_3@GO hybrids

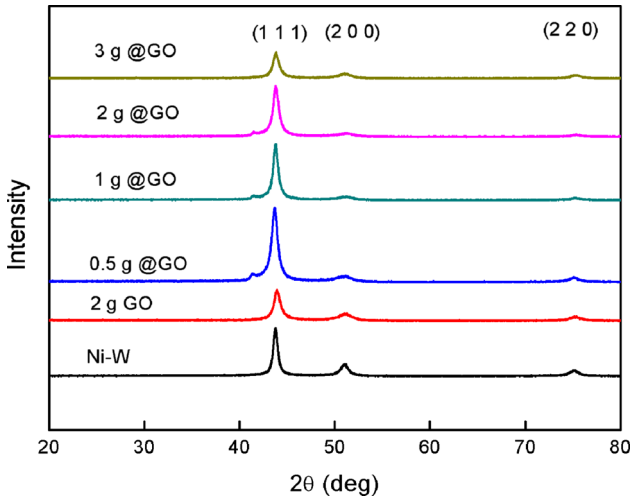

Fig. 8. XRD patterns of composite coatings

(Table 2) which showed that composite coatings displayed the smallest crystallites when the content of Al_2O_3@GO was 1 g L^{-1} in the plating bath. Crystallite refinement occurred because metal ions and complexes in the plating bath were adsorbed by GO or Al_2O_3@GO (Ref 51) which inhibited the growth of crystal nuclei. The rate of nucleation was increased by GO through the growth of Ni-W centers, which prevented the growing metal surface (Ref 16).

3.2.2 SEM and EDS Analysis. Figure 9 shows the SEM micrographs of all composite coatings. A typical cauliflower-type morphology was obtained on the Ni-W coating surface, as shown in Fig. 9(a). No microcracks were observed on the surface, and the W content was about 22.16 wt.%. When the GO sheets were added into the Ni-W coating, the nodular morphology becomes smoother (Fig. 9b). The higher magnification SEM image shows that graphene sheets were homogeneously dispersed in the coatings. The C content was about 6.29 wt.%, as indicated by wave-dispersive spectrometry (WDS).

Figure 9(c, d, e, f) shows that the surfaces of Ni-W-Al_2O_3@GO coatings were rougher than the Ni-W-GO composite coating; however, there were only a few bare Al_2O_3@GO. Figure 9(c) shows that homogeneous nodulations were distributed on the smooth surface in the Ni-W-Al_2O_3@GO coating when the Al_2O_3@GO content in the plating solution was 0.5 g L^{-1}. WDS analysis showed that the nodulations were the cladded Al_2O_3@GO, corresponding to the C content of 29.29 wt.%, compared with 1.35 wt.% in the smooth areas. At a lower content of Al_2O_3@GO, an open pore structure was formed due to the interconnection of GO sheets. This provided a short-cut path for the insertion and extraction of electrolyte ions into the surface of GO (Ref 52). The electrolyte ions quickly penetrated and accumulated on the surface of Al_2O_3@GO and then formed a small number of nodulations on the coating surface.

Upon increasing the Al_2O_3@GO content, the nodulations were compacted and homogeneous, as displayed in Fig. 9(d, e). However, when the concentration of Al_2O_3@GO increased to 3 g L^{-1}, the surface morphology was the same as that of the 0.5 g L^{-1} concentration (Fig. 9f). The carbon contents were about 6.10 wt.%, 18.18 wt.%, 22.21 wt.%, and 7.89 wt.%, which corresponded to Al_2O_3@GO concentrations in the plating solution of 0.5 g L^{-1}, 1 g L^{-1}, 2 g L^{-1}, and 3 g L^{-1}, respectively. This indicates that the Al_2O_3@GO content in the coating did not always improve upon increasing the Al_2O_3@-GO content in the plating solution. EDS mapping analysis of the Ni-W-Al_2O_3@GO (1 g L^{-1}) composite coating surface in Fig. 9(g) shows that Al_2O_3@GO was uniformly distributed throughout the coatings, which indicates that Al_2O_3@GO may be well dispersed in the plating solution.

The cross-sectional morphologies of the Ni-W-Al_2O_3@GO coatings in Fig. 10 show that the composite coatings were well-bonded to the substrate with no visible defects and cracks at the interface. The composite coatings showed a compact microstructure and high bonding strength upon the addition of 0.5 g L^{-1} (Fig. 10a) and 1 g L^{-1} (Fig. 10b) Al_2O_3@GO. However, the cross-sectional structure of the Ni-W-Al_2O_3@GO coating is separated with 2 g L^{-1} Al_2O_3@GO in the plating solution, as displayed in Fig. 10c. Defects appeared on the external surface of the coating, and when the concentration of Al_2O_3@GO increased to 3 g L^{-1} the coating showed obvious defects and cracks (Fig. 10d).

The EDS line scanning analysis for Ni-W-Al_2O_3@GO composite coating (1 g L^{-1}) (Fig. 11) shows that the coating contains three major components: Ni, W, and C. The mapping of the cross section supports the line scanning results. The EDS mapping analysis of the coating surfaces shows the presence of carbon, which indicates that Al_2O_3@GO was uniformly distributed as thin sheets embedded in the composite coatings. This further confirmed that Al_2O_3@GO exhibited a better dispersion in the plating bath.

3.2.3 Raman Spectra. In order to investigate the state of Al_2O_3@GO in the composite coatings, Raman spectra were obtained. The D-band (1360 cm^{-1}) and G-band (1600 cm^{-1})

Table 2 The grain sizes of composite coatings

Coatings	Ni-W	Ni-W-GO	Ni-W-@GO, 0.5 g L^{-1}	Ni-W-@GO, 1 g L^{-1}	Ni-W-@GO, 2 g L^{-1}	Ni-W-@GO, 3 g L^{-1}
Grain size, nm	45.2	29.6	13.4	8	11.4	14.1

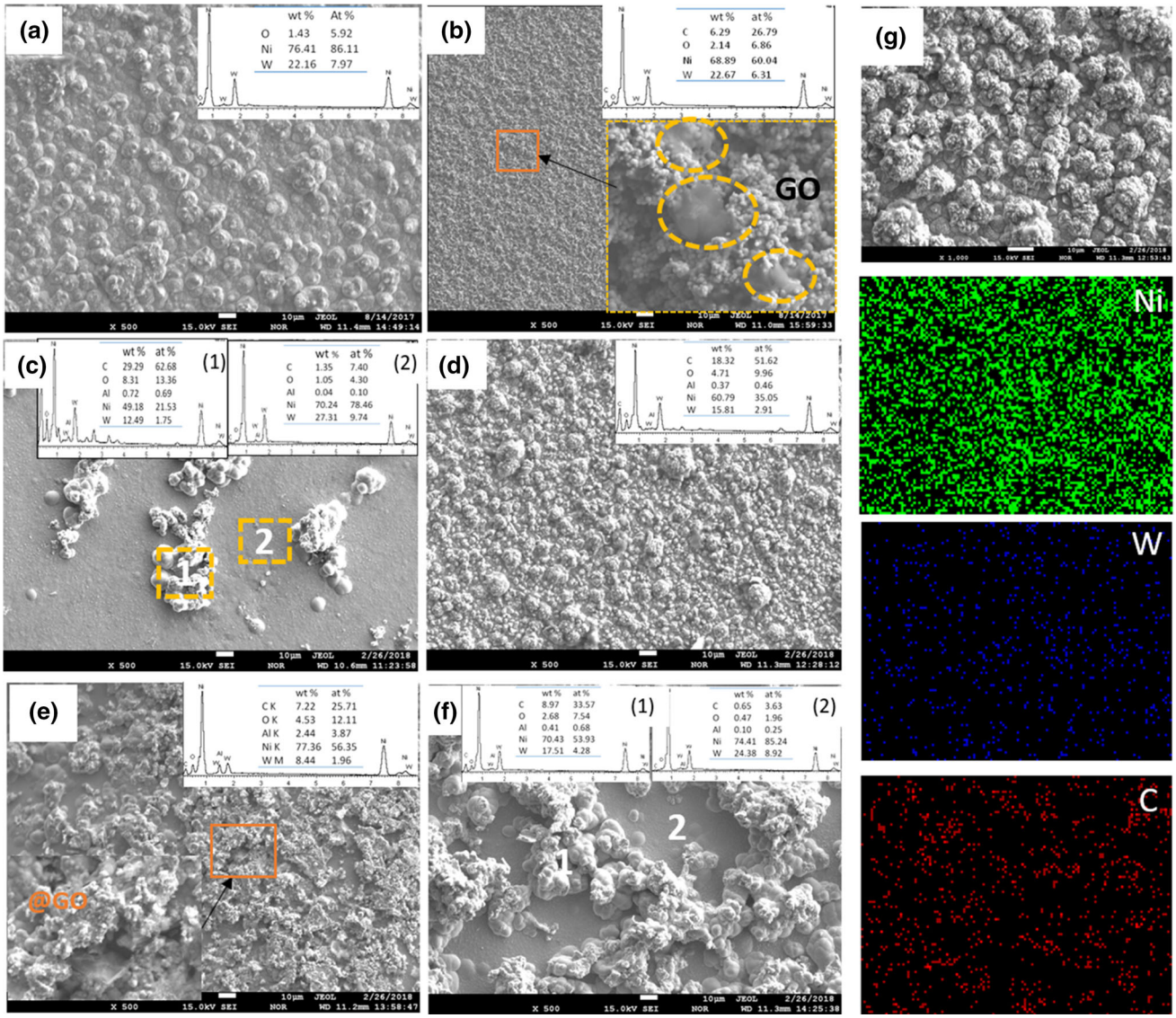

Fig. 9. SEM photomicrographs of composite coatings (a) Ni-W, (b) Ni-W-GO, (c) Ni-W-Al_2O_3@GO 0.5 g L^{-1}, (d) Ni-W-Al_2O_3@GO 1 g L^{-1}, (e) Ni-W-Al_2O_3@GO 2 g L^{-1}, (f) Ni-W-Al_2O_3@GO 3g L^{-1}

were observed in all Ni-W-Al_2O_3@GO coatings, as shown in Fig. 12. Compared with Al_2O_3@GO (Fig. 5), the I_D/I_G ratios all increased, which confirms that Al_2O_3@GO was introduced into the composite coatings successfully and was reduced during the process of electrodeposition.

3.3 Corrosion Performance

The polarization curves of all composite coatings are displayed in Fig. 13. The corrosion potential (E_{corr}) and current density (i_{corr}) obtained from Tafel plot extrapolation are listed in Table 3. The coatings formed from plating solutions containing 1 g L^{-1} of GO and 0.5 g L^{-1}, 1 g L^{-1}, 2 g L^{-1} of Al_2O_3@GO possessed higher E_{corr} and lower i_{corr} values than the Ni-W composite coatings. More importantly, at an Al_2O_3@GO sheet content of 1 g L^{-1} in the plating solution, E_{corr} significantly increased, while i_{corr} sharply decreased. But, the corrosion marginally increased at 3 g L^{-1} Al_2O_3@GO. Figure 9 shows that the composite coatings contained defects and cracks at the interface, which reduced their corrosion resistance (Ref 21, 53).

To better understand the corrosion resistance of the composite coatings, EIS was performed. Figure 14 illustrates the Nyquist plots of all coatings, which all show a single semi-

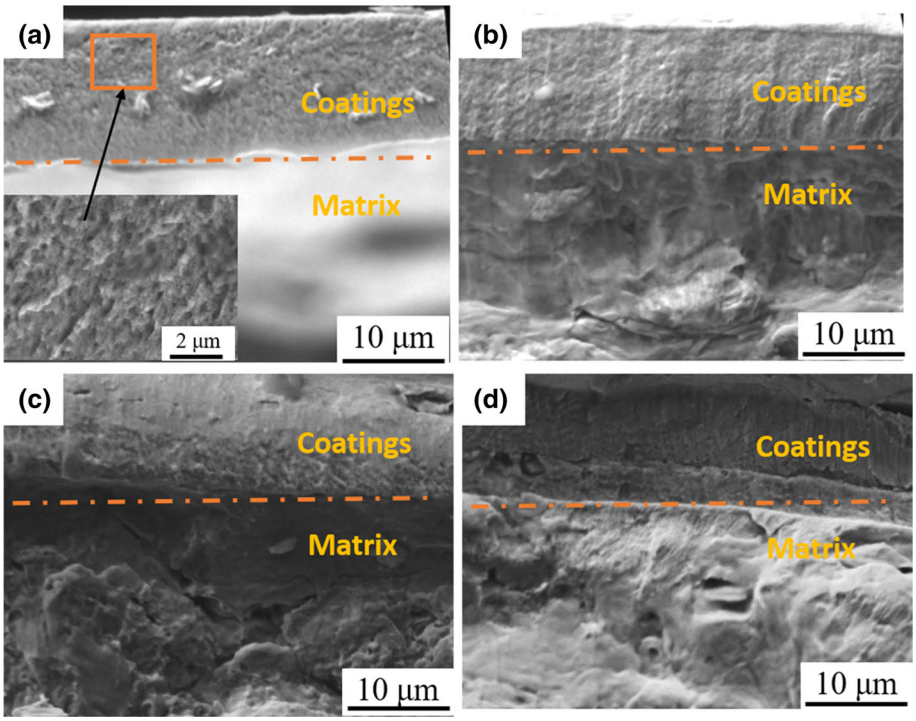

Fig. 10. Cross-sectional images of Ni-W-Al_2O_3@GO composite coatings with (a) 0.5 g L^{-1}, (b) 1 g L^{-1}, (c) 2 g L^{-1}, (d) 3 g L^{-1} Al_2O_3@GO in the plating solution

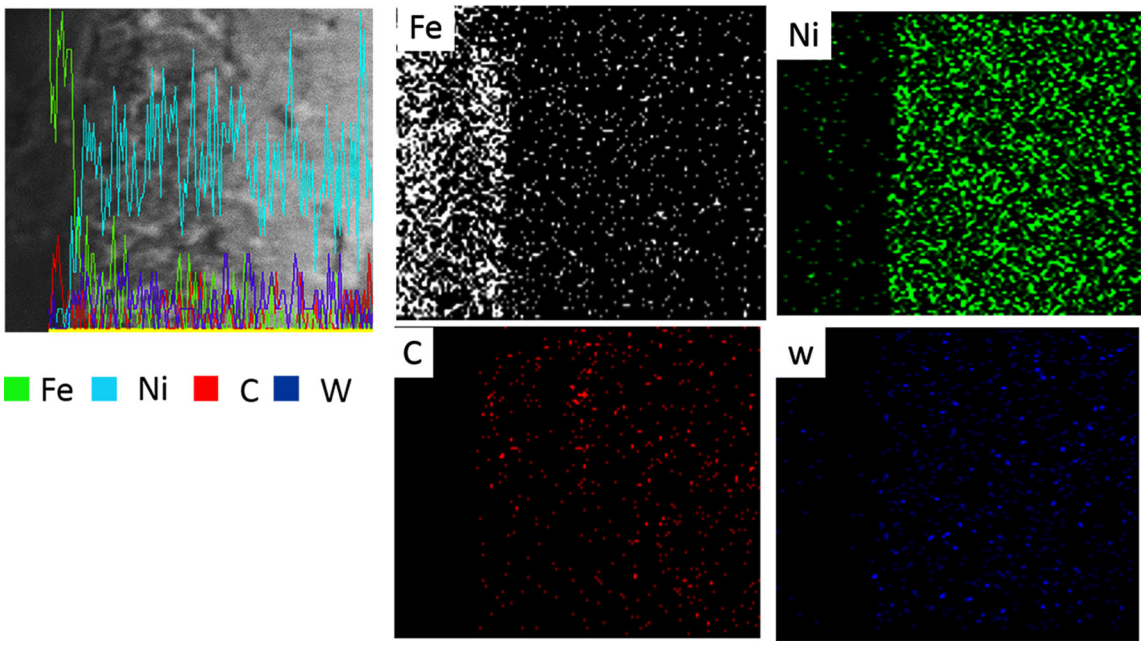

Fig. 11. Line scanning and elemental mapping of a cross section of the Ni-W-Al_2O_3@GO composite coating (1 g L^{-1})

circular arc. In contrast to the others, the Ni-W-Al_2O_3@GO composite coating produced at 1 g L^{-1} Al_2O_3@GO content in the plating solution showed a remarkably larger semi-circular arc. The observed results imply the presence of an equivalent circuit composed of 2RQ components, with the electrochemical parameters listed in Table 4. The Ni-W-Al_2O_3@GO coatings displayed a higher charge transfer resistance (R_{ct}) and lower double-layer capacitance (CPE_{dl}). The addition of Al_2O_3@GO sheets to the Ni-W composite coating lowered the CPE_{dl} and increased R_{ct} which decreased i_{corr} consistent with the results of polarization.

The addition of GO formed coatings with more compact microstructures due to grain refinement and the presence of fewer defects. The anti-corrosion properties of the coatings were improved because the well-dispersed rGO served as a barrier to corrosive media (Ref 34). However, the embedded rGO is cathodic to most metallic materials due to a more positive electrode potential (Ref 54). For the exposed

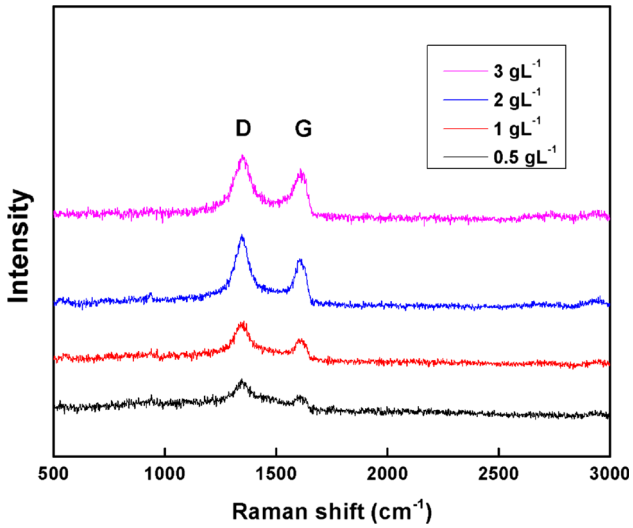

Fig. 12. Raman spectra of Ni-W-Al_2O_3@GO composite coatings

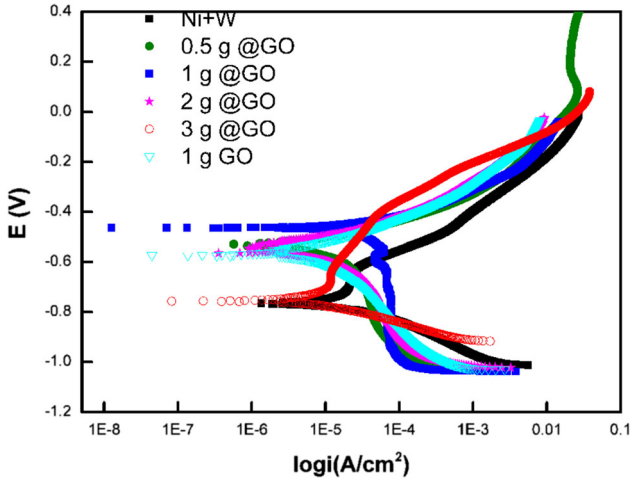

Fig. 13. Polarization curves of the composite coatings

Table 3 Corrosion potentials and corrosion current densities of the composite coatings

Sample	Ecorr, mV	Icorr, μA
Ni-W	−763	6.66
Ni-W-GO	−573	0.706
Ni-W-Al_2O_3@GO, 0.5 g L^{-1}	−528.9	0.65
Ni-W-Al_2O_3@GO, 1 g L^{-1}	−464.3	0.195
Ni-W-Al_2O_3@GO, 2 g L^{-1}	−564.8	0.437
Ni-W-Al_2O_3@GO, 3 g L^{-1}	−757	4.19

graphene–metal interfaces (bare rGO as shown in Fig. 9b), rGO accelerated localized corrosion (Ref 38, 55), which decreased the corrosion resistance of the barrier layer.

The corrosion test results showed that the corrosion resistance of Ni-W-Al_2O_3@GO composite coating formed from 1 g L^{-1} Al_2O_3@GO in the plating solution was enhanced compared with that of Ni-W-GO. The electrical conductivities of RGO and rAl_2O_3@GO were measured using a four-point probe setup and were found to be 4081 S m^{-1}, 1.31 S m^{-1},

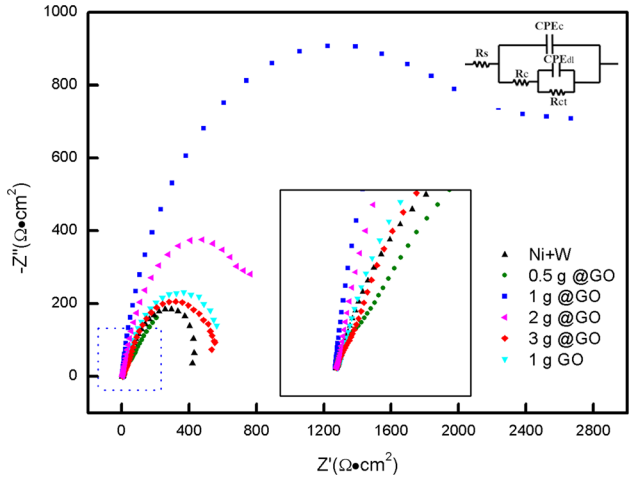

Fig. 14. Nyquist plots of the composite coatings

respectively. The FTIR spectra of RGO and rAl_2O_3@GO are shown in Fig. 6. The GO peaks completely disappeared in the FTIR spectrum of R@GO, but the hydroxyl (3430 cm^{-1}), C-H bending, N-H rocking, and Si-O-Al stretching peaks remained. The conductivity of rAl_2O_3@GO was less than 3 S m^{-1} due to the adsorption of an insulating surfactant layer (Ref 56, 57). The addition of insulating R@GO sheets resulted in a higher corrosion resistance than the Ni-W-GO coating.

The mechanism responsible for the improved anti-corrosion behavior of the R@GO sheets is shown in Fig. 15. First, the coating microstructure became more compact due to grain refinement and fewer defects, making it difficult for the corrosive media to enter the coatings. Secondly, the well-dispersed Al_2O_3@GO sheets in the coating provided a barrier that prevented the penetration of corrosive mediators into the micropores or microcracks. Finally, the insulating R@GO sheets embedded in coatings prevented the formation of primary cells of the coated metal, blocked the electron transfer path, and reduced the cathodic area (Ref 51).

3.4 Tribological properties of composite coatings

The coefficient of friction (COF) as a function of time for Ni-W, Ni-W-GO, and Ni-W-Al_2O_3@GO composite coatings via a sliding speed of 10 mm s^{-1} under loads of 1 N is presented in Fig. 16. The COF curve of the Ni-W coating continually increases from 0.33 to 0.58 over time. Similarly, the COF curves of Ni-W-GO and Ni-W-Al_2O_3@GO composite coatings (0.5 g L^{-1}, 3 g L^{-1}) also continually increase to 0.48 before stabilizing. Furthermore, the COF value of Ni-W-Al_2O_3@GO coatings produced with 1 g L^{-1} Al_2O_3@GO in the plating solution stabilized at the lowest value of 0.38.

The COF curves of Ni-W-Al_2O_3@GO with 1 g L^{-1} at different sliding speeds and contact loads are displayed in Fig. 17. Under a load of 10 N, the COF curve became smoother and eventually stabilized around 0.36. With a sliding speed of 20 mm/s, the COF quickly increased during the initial stage, before beginning to decrease at 1800 s, then settling around 0.4. These results show that the 1 g L^{-1} Ni-W-Al_2O_3@GO coating displayed a better friction reduction than the Ni-W-GO coating.

A general view of the wear tracks of the Ni-W-Al_2O_3@GO composite coatings is displayed in Fig. 18. Deeper abrasive grooves with wider wear tracks occur in the worn surface of the 0.5 g L^{-1} Ni-W-Al_2O_3@GO composite coatings, as shown in

Table 4 Equivalent circuit fit parameters for the EIS samples

Sample	Rct, Ω·cm^2	Rc, Ω·cm^2	CPE_{dl}, F	CPE_c, F
Ni-W	515.8	721.7	3.846×10^{-3}	1.266×10^{-3}
Ni-W-GO	696	828.2	2.9×10^{-3}	1.05×10^{-3}
Ni-W-Al_2O_3@GO, 0.5 g L^{-1}	978.3	1002	1.766×10^{-3}	0.430×10^{-3}
Ni-W-Al_2O_3@GO, 1 g L^{-1}	2445	2675	0.359×10^{-3}	0.567×10^{-3}
Ni-W-Al_2O_3@GO, 2 g L^{-1}	965	974.8	1.38×10^{-3}	1.988×10^{-3}
Ni-W-Al_2O_3@GO, 3 g L^{-1}	506	766	2.97×10^{-3}	1.38×10^{-3}

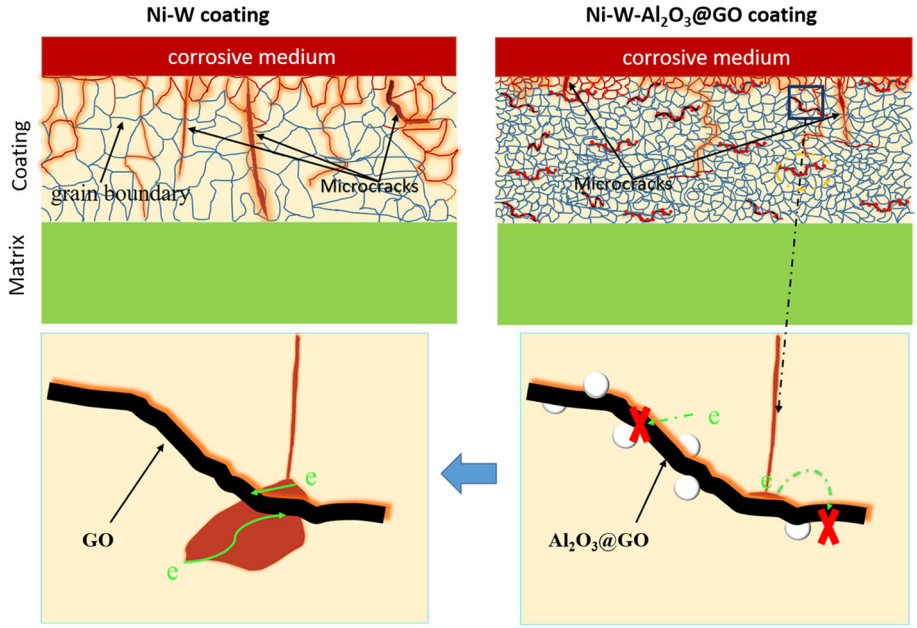

Fig. 15. Schematic representation of the anti-corrosion mechanisms of Ni-W-Al_2O_3@GO composite coatings

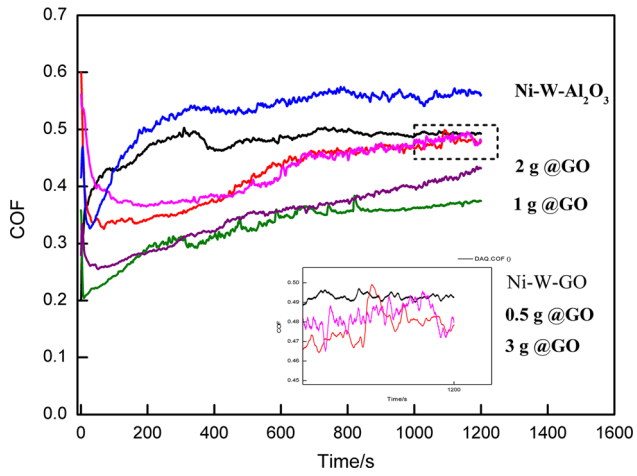

Fig. 16. Coefficient of friction of composite coatings vs time under loads of 1 N and sliding speed of 10 mm/s

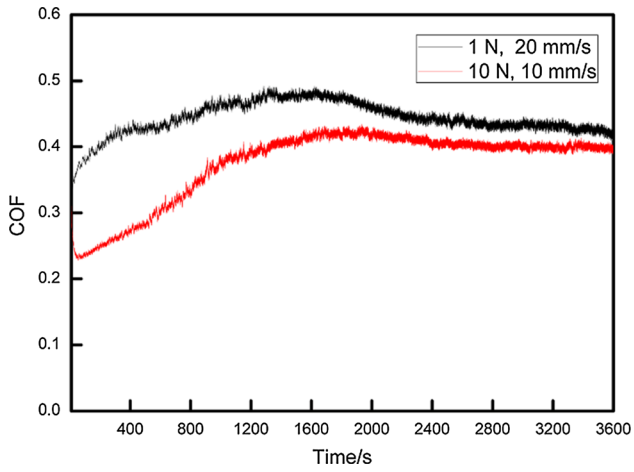

Fig. 17. Coefficient of friction of Ni-W-Al_2O_3@GO composite coating via 1 g L^{-1}

Fig. 18(a). The small clusters distributed on the rough coating surface were first rubbed off during the initial stage of wear, which may have caused the COF to fluctuate. The worn surfaces of composite coatings via 2 g L^{-1} and 3 g L^{-1} Al_2O_3@GO show wider wear tracks with clear scuffing due to the rough surface. The wear track of the 1 g L^{-1} Ni-W-Al_2O_3@GO composite coating shows mild abrasive wear with shallow plowing and a narrower wear track.

The SEM morphologies of the worn surface of Ni-W-Al_2O_3@GO composite coating via 1 g L^{-1} after sliding for 3600 s are shown in Fig. 19. When the sliding speed was increased to 20 mm/s, the wear track became very smooth with

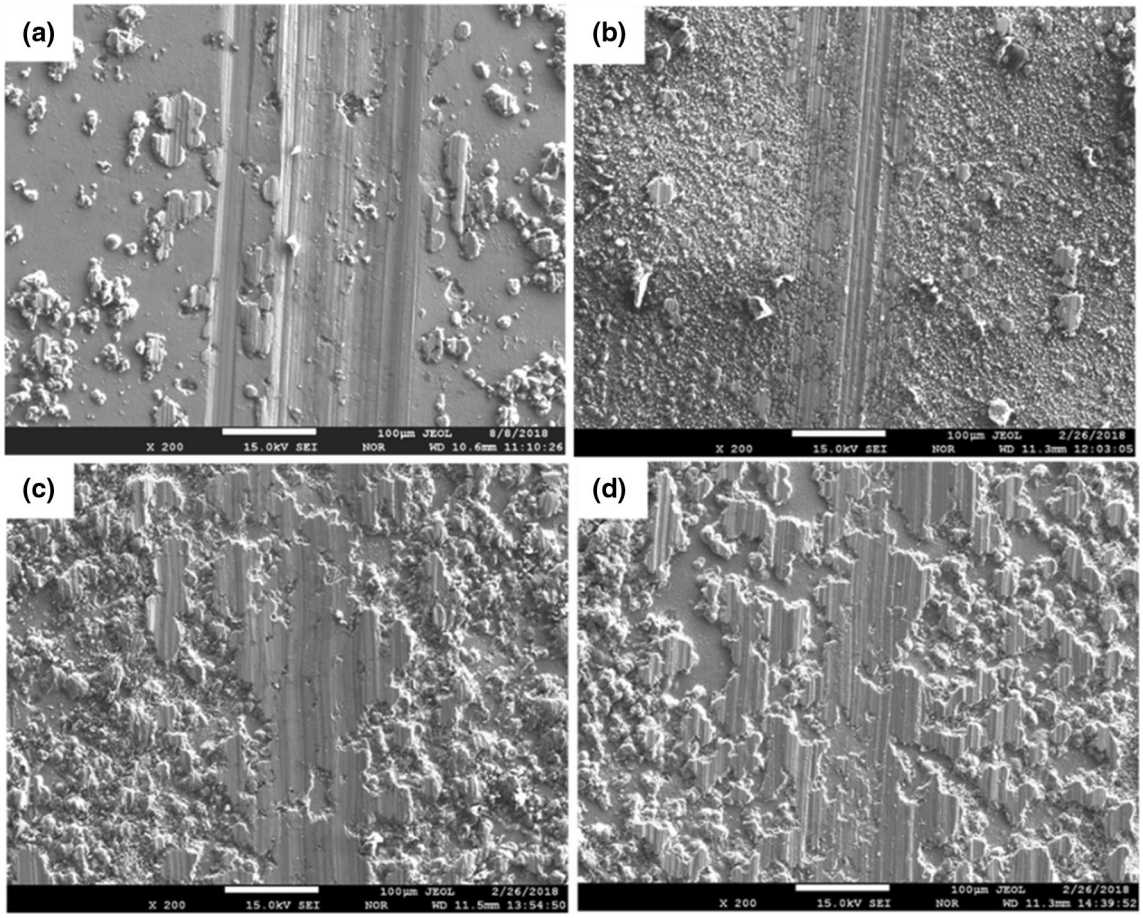

Fig. 18. SEM morphology of the wear surface of Ni-W-Al_2O_3@GO composite coatings via 1 N and 10 mm/s. (a) 0.5 g L^{-1}, (b) 1 g L^{-1}, (c) 2 g L^{-1}, (d) 3 g L^{-1}

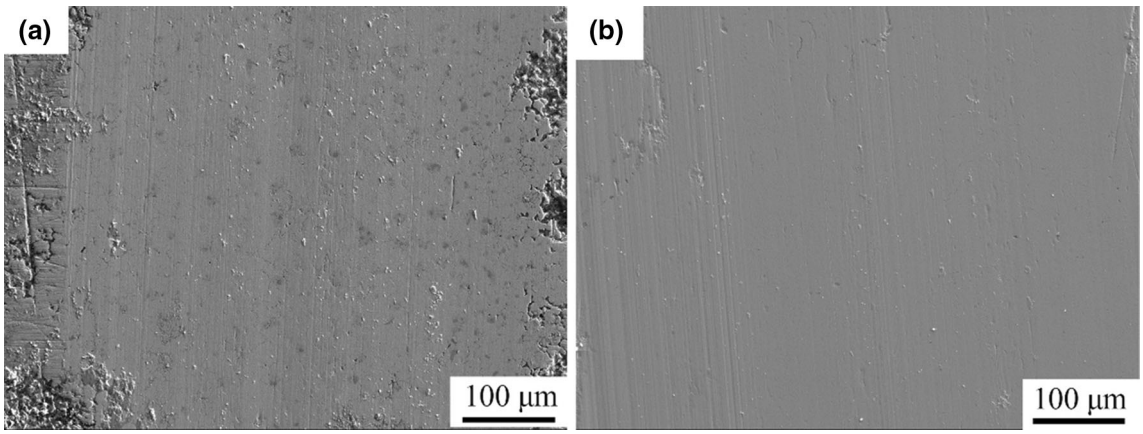

Fig. 19. SEM morphology of the worn surface of Ni-W-Al_2O_3@GO composite coating (1 g L^{-1}). (a) 1 N and 20 mm/s, (b) 10 N and 10 mm/s

only slight plowing (Fig. 19a), due to the longer sliding time and higher speeds which rapidly removed the bulges and filled holes with wear debris. At a load of 10 N, the worn surface became smoother and wider, as shown in Fig. 19(b). Ni-W-Al_2O_3@GO composite coating via a 1 g L^{-1} content in the plating solution had a low friction coefficient and good wear resistance at different sliding speeds and contact loads.

The Ni-W coatings embedded with 1 g L^{-1} Al_2O_3@GO sheets showed a rougher surface than the one with embedded GO sheets; however, it had better anti-friction and wear resistance than the Ni-W-GO coating. The Al_2O_3@GO content in the plating bath had an important impact on the microstructure and performance of the composite coatings. The anti-wear mechanism involved load transmission from the matrix by the

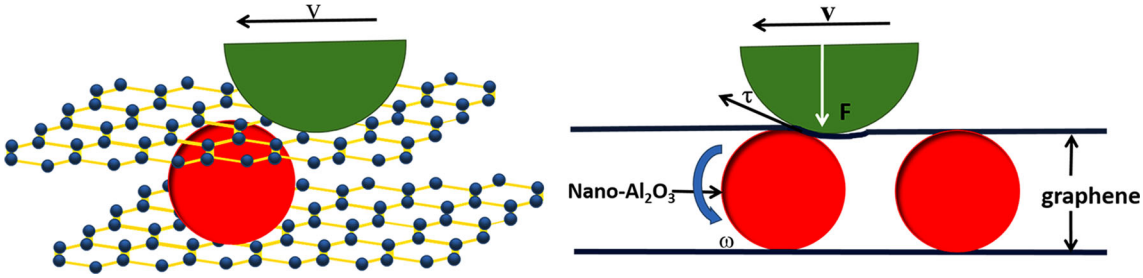

Fig. 20. Schematic representation of the anti-friction mechanisms of Ni-W-Al_2O_3@GO composite coatings

GO sheets which decreased the shear forces acting on the contact face because the coatings slightly bulged out (Ref 34). Similarly, the Al_2O_3@GO sheets decreased the shear forces acting on the contact face by supporting the loads transmitted from the matrix. The schematic of this similar "bearing" mechanism is shown in Fig. 20. Al_2O_3 nanoparticles cladded with GO sheets may rotate under the action of tangential forces τ (a component of friction), and the Al_2O_3@GO sheets play a role similar to "rolling." The wear mode of the coating transformed from sliding to rolling, which improved the anti-wear performance and reduced the COF of the coatings.

4. Conclusion

Ni-W coatings with low friction coefficients and anti-corrosion properties were fabricated by embedding Al_2O_3@GO sheets, and the coating with 1 g L^{-1} of GO addition displayed better corrosion on and wear resistance properties than Ni-W coating, Ni-W-GO coating, and other Ni-W-Al_2O_3@GO coatings due to grain refinement and fewer defects.

The cross-linking between the metal and carboxylic acid groups of GO sheets in the plating bath was prevented by removing the carboxylic acids during the modification by Al_2O_3 nanoparticles. Moreover, the FTIR spectrum of R@GO showed that retaining the other oxygen functional groups on the surface of R@GO sheets. Which ensured that Al_2O_3@GO remained well dispersed during the plating process, and the good dispersibility of Al_2O_3@GO sheets in the Ni-W plating bath ensured they were well dispersed in the coating.

The R@GO sheets served as an insulating barrier which made it difficult for corrosive media to penetrate the coatings. Additionally, the insulation of the R@GO sheets blocked electron transfer pathways and reduced the cathodic area compared with RGO sheets. By supporting the loads transmitted from the matrix, which decreased the shear forces on the contact face, the R@GO sheets improved the anti-friction property and wear resistance of the coating. We expect that this GO modification procedure can be applied to reinforce metal composite coatings, and this study may open up a new method for preparing metal–graphene composite coatings.

Acknowledgments

The authors are thankful for funding from National Natural Science Foundation of China (Nos. 51772176, 51971121), Taishan Scholarship of Climbing Plan (No. tspd20161006), and Shandong Province Key Laboratory of Mine Mechanical Engineering (No. 2019KLMM101).

Author Contributions

G.Z. and H.C. contributed to conception; G.Z. and X.S. contributed to experimental design; G.Z., X.S., and S.T carried out measurements.; G.Z. and C.S. contributed to manuscript composition.

Conflict of interest

To the best of our knowledge, the named authors have no conflict of interest, financial or otherwise.

References

1. B.L. Hung, Synergy Between Corrosion and Wear of Electrodeposited Ni-W Coating, *Tribol. Lett.*, 2013, **50**, p 407–415. https://doi.org/10.1007/s11249-013-0134-x
2. S. Yari and C. Dehghanian, Deposition and Characterization of Nanocrystalline and Amorphous Ni-W Coatings with Embedded Alumina Nanoparticles, *Ceram. Int.*, 2013, **39**, p 7759–7767. https://doi.org/10.1016/j.ceramint.2013.03.033
3. X.Q. Fang, Y. Zhang, K.G. Zhu et al., Surface Morphology and Crystal Orientation of Electrodeposited Tungsten Coatings with Different Pulse Parameters, *Rare Met.*, 2018, **37**, p 407–418. https://doi.org/10.1007/s12598-016-0825-1
4. N. Eliaz, T.M. Sridhar and E. Gileadi, Synthesis and Characterization of Nickel Tungsten Alloys by Electrodeposition, *Electrochim. Acta*, 2005, **50**, p 2893–2904. https://doi.org/10.1016/j.electacta.2004.11.038
5. K.A. Kumar, G.P. Kalaignan and V.S. Muralidharan, Pulse Electrodeposition and Characterization of Nano Ni-W Alloy Deposits, *Appl. Surf. Sci.*, 2012, **259**, p 231–237. https://doi.org/10.1016/j.apsusc.2012.07.024
6. J. Lee, C.R. Lear, X. Zhang, P. Bellon and R.S. Averback, Irradiation-Induced Nanoprecipitation in Ni-W Alloys, *Metall. Mater. Trans. A*, 2015, **46A**, p 1046–1061. https://doi.org/10.1007/s11661-014-2704-4
7. S. Kabi, K. Raeissi and A. Saatchi, Effect of Polarization Type on Properties of Ni-W Nanocrystalline Electrodeposits, *J. Appl. Electrochem.*, 2009, **39**, p 1279–1285. https://doi.org/10.1007/s10800-009-9796-3
8. K.R. Sriraman, S.G. Raman and S.K. Seshadri, Corrosion Behaviour of Electrodeposited Nanocrystalline Ni-W and Ni-Fe-W Alloys, *Mater. Sci. Eng.: A*, 2007, **460–461**, p 39–45. https://doi.org/10.1016/j.msea.2007.02.055
9. G. Gyawali, B. Joshi, K. Tripathi and S.W. Lee, Preparation of Ni-W-Si_3N_4 Composite Coatings and Evaluation of Their Scratch Resistance Properties, *Ceram. Int.*, 2016, **42**, p 3497–3506. https://doi.org/10.1016/j.ceramint.2015.10.153
10. M.H. Allahyarzadeh, M. Aliofkhazraei, A.R.S. Rouhaghdam and V. Torabinejad, Electrodeposition of Ni-W-Al_2O_3 Nanocomposite Coating

with Functionally Graded Microstructure, *J. Alloys Compd.*, 2016, **666**, p 217–226. https://doi.org/10.1016/j.jallcom.2016.01.031
11. E. Beltowska-Lehman, P. Indyka, A. Bigos, M. Kot and L. Tarkowski, Electrodeposition of Nanocrystalline Ni-W Coatings Strengthened by Ultrafine Alumina Particles, *Surf. Coat. Technol.*, 2012, **211**, p 62–66. https://doi.org/10.1016/j.surfcoat.2011.10.021
12. K.H. Hou and Y.C. Chen, Preparation and Wear Resistance of Pulse Electrodeposited Ni-W/Al_2O_3 Composite Coatings, *Appl. Surf. Sci.*, 2011, **257**, p 6340–6346. https://doi.org/10.1016/j.apsusc.2011.01.089
13. K.A. Kumar, G.P. Kalaignan and V.S. Muralidharan, Direct and Pulse Current Electrodeposition of Ni-W-TiO_2 Nanocomposite Coatings, *Ceram. Int.*, 2013, **39**, p 827–2834. https://doi.org/10.1016/j.ceramint.2012.09.054
14. Y. Wang, Q. Zhou, K. Li, Q. Zhong and Q.B. Bui, Preparation of Ni-W-SiO_2 Nanocomposite Coating and Evaluation of Its Hardness and Corrosion Resistance, *Ceram. Int.*, 2015, **41**, p 79–84. https://doi.org/10.1016/j.ceramint.2014.08.034
15. E. Beltowska-Lehman, P. Indyka, A. Bigos, M.J. Szczerba, J. Guspiel, H. Koscielny and M. Kot, Effect of Current Density on Properties of Ni-W Nanocomposite Coatings Reinforced with Zirconia Particles, *Mater. Chem. Phys.*, 2016, **173**, p 524–533. https://doi.org/10.1016/j.matchemphys.2016.02.050
16. H. Li, Y. He, T. He, Y. Fan, Q.B. Yang and Y.Q. Zhan, The Influence of Pulse Plating Parameters on Microstructure and properties of Ni-W-Si_3N_4 Nanocomposite Coatings, *Ceram. Int.*, 2016, **42**, p 18380–18388. https://doi.org/10.1016/j.ceramint.2016.08.171
17. B. Li, W. Zhang, W. Zhang and Y. Huan, Preparation of Ni-W/SiC Nanocomposite Coatings by Electrochemical Deposition, *J. Alloys Compd.*, 2017, **702**, p 38–50. https://doi.org/10.1016/j.jallcom.2017.01.239
18. Y. Boonyongmaneerat, K. Saengkiettiyut, S. Saenapitak and S. Sangsuk, Effects of WC Addition on Structure and Hardness of Electrodeposited Ni-W, *Surf. Coat. Technol.*, 2009, **203**, p 3590–3594. https://doi.org/10.1016/j.surfcoat.2009.05.027
19. K.H. Hou, T. Han, H.H. Sheu and M.D. Ger, Preparation and Wear Resistance of Electrodeposited Ni-W/Diamond Composite Coatings, *Appl. Surf. Sci.*, 2014, **308**, p 372–379. https://doi.org/10.1016/j.apsusc.2014.04.175
20. S. Das, P. Singh and K.M.K. Srivatsa, Synthesis of CeO_2 Microcrystals Fabricated on Biaxially Textured Ni-W Substrate by Using an E-Beam Evaporation Technique, *J. Korean Phys. Soc.*, 2015, **66**, p 726–729. https://doi.org/10.3938/jkps.66.726
21. T. He, Y. He, H. Li, Y. Fan, Q. Yang and Z. He, A Comparative Study of Effect of Mechanical and Ultrasound Agitation on the Properties of Pulse Electrodeposited Ni-W/MWCNTs Composite Coatings, *J. Alloys Compd.*, 2018, **743**, p 63–72. https://doi.org/10.1016/j.jallcom.2018.01.368
22. H. Li, Y. He, T. He, D. Qing, F. Luo, Y. Fan and X. Chen, Ni-W/BN(h) Electrodeposited Nanocomposite Coating with Functionally Graded Microstructure, *J. Alloys Compd.*, 2017, **704**, p 32–43. https://doi.org/10.1016/j.jallcom.2017.02.037
23. A.K. Geim and K.S. Novoselov, The Rise of Grapheme, *Nat. Mater.*, 2007, **6**, p 183–191. https://doi.org/10.1038/nmat1849
24. M. Belmonte, C. Ramírez, J. González-Julián, J. Schneider, P. Miranzo and M.I. Osendi, The Beneficial Effect of Graphene Nanofillers on the Tribological Performance of Ceramics, *Carbon*, 2013, **61**, p 431–435. https://doi.org/10.1016/j.carbon.2013.04.102
25. S. Liu, J. Ou, Z. Li, S. Yang and J. Wang, Layer-by-Layer Assembly and Tribological Property of Multilayer Ultrathin Films Constructed by Modified Graphene Sheets and Polyethyleneimine, *Appl. Surf. Sci.*, 2012, **258**, p 2231–2236. https://doi.org/10.1016/j.apsusc.2011.09.011
26. A. Siokou, F. Ravani, S. Karakalos, O. Frank, M. Kalbac and C. Galiotis, Surface Refinement and Electronic Properties of Graphene Layers Grown on Copper Substrate: An XPS, UPS and EELS Study, *Appl. Surf. Sci.*, 2011, **257**, p 9785–9790. https://doi.org/10.1016/j.apsusc.2011.06.017
27. J. Yang and L. Zou, Graphene Films of Controllable Thickness as Binder-Free Electrodes for High Performance Supercapacitors, *Electrochim. Acta*, 2014, **130**, p 791–799. https://doi.org/10.1016/j.electacta.2014.03.077
28. C.M. Praveen Kumar, T.V. Venkatesha and R. Shabadi, Preparation and Corrosion Behavior of Ni and Ni-Graphene Composite Coatings, *Mater. Res. Bull.*, 2013, **48**, p 1477–1486. https://doi.org/10.1016/j.materresbull.2012.12.064
29. D. Kuang, L. Xu, L. Liu, W. Hu and Y. Wu, Graphene-Nickel Composites, *Appl. Surf. Sci.*, 2013, **273**, p 484–490. https://doi.org/10.1016/j.apsusc.2013.02.066
30. J. Chen, J. Li, D. Xiong, Y. He, Y. Ji and Y. Qin, Preparation and Tribological Behavior of Ni-Graphene Composite Coating Under Room Temperature, *Appl. Surf. Sci.*, 2016, **361**, p 49–56. https://doi.org/10.1016/j.apsusc.2015.11.094
31. A. Siokou, F. Ravani, S. Karakalos, O. Frank, M. Kalbac and C. Galiotis, Surface Refinement and Electronic Properties of Graphene Layers Grown on Copper Substrate: An XPS, UPS and EELS Study, *Appl. Surf. Sci.*, 2012, **257**, p 9785–9791. https://doi.org/10.1016/j.apsusc.2015.11.094
32. N.A. Kotov, I. Dekany and J.H. Fendler, Ultrathin Graphite Oxide-Polyelectrolyte Composites Prepared by Self-Assembly: Transition Between Conductive and Non-Conductive States, *Adv. Mater.*, 1996, **8**, p 637–641. https://doi.org/10.1002/adma.19960080806
33. T. Szabo, A. Szeri and I. Dekany, Composite Graphitic Nanolayers Prepared by Self-Assembly Between Finely Dispersed Graphite Oxide and a Cationic Polymer, *Carbon*, 2005, **43**, p 87–94. https://doi.org/10.1016/j.carbon.2004.08.025
34. Y. Fan, Y. He, P.Y. Luo, T.H. Shi and X. Chen, Pulse Current Electrodeposition and Properties of Ni-W-GO Composite Coating, *J Electrochem Soc.*, 2016, **163**, p 68–75. https://doi.org/10.1149/2.0171603jes
35. X. Zhang, X. Li, W. Liu, Y. Fan, H. Chen and T. Liang, Preparation and Tribological Behavior of Electrodeposited Ni-W-GO Composite Coatings, *Rare Met.*, 2018 https://doi.org/10.1007/s12598-018-1173-0
36. S. Park, K.-S. Lee, G. Bozoklu, W. Cai, S.T. Nguyen and R.S. Ruoff, Graphene Oxide Papers Modified by Divalent Ions-Enhancing Mechanical Properties via Chemical Cross-Linking, *ACS Nano*, 2008, **2**, p 572–579. https://doi.org/10.1021/nn700349a
37. S. Arora and C. Srivastava, Microstructure and Corrosion Properties of NiCo-Graphene Oxide Composite Coatings, *Thin Solid Films*, 2019, **677**, p 45–54. https://doi.org/10.1016/j.tsf.2019.03.011
38. M. Schriver, W. Regan, W.J. Gannett, A.M. Zaniewski, M.F. Crommie and A. Zettl, Graphene as a Long-Term Metal Oxidation Barrier: Worse than Nothing, *ACS Nano*, 2013, **7**, p 5763–5768. https://doi.org/10.1021/nn4014356
39. Z. Yu, H. Di, Y. Ma, Y. He, L. Liang, L. Lv, X. Ran, Y. Pan and Z. Luo, Preparation of Graphene Oxide Modified by Titanium Dioxide to Enhance the Anti-Corrosion Performance of Epoxy Coatings, *Surf. Coat. Technol.*, 2015, **276**, p 471–478. https://doi.org/10.1016/j.surfcoat.2015.06.027
40. Z. Yu, H. Di, Y. Ma et al., Fabrication of Graphene Oxide-Alumina Hybrids to Reinforce the Anti-Corrosion Performance of Composite Epoxy Coatings, *Appl. Surf. Sci.*, 2015, **351**, p 986–996. https://doi.org/10.1016/j.apsusc.2015.06.026
41. Y. Ma, H. Di, Z. Yu, L. Liang, L. Lv, Y. Pan, Y. Zhang and D. Yin, Fabrication of Silica-Decorated Graphene Oxide Nanohybrids and the Properties of Composite Epoxy Coatings Research, *Appl. Surf. Sci.*, 2016, **360**, p 936–945. https://doi.org/10.1016/j.apsusc.2015.11.088
42. S. Pourhashem, M.R. Vaezi and A. Rashidi, Investigating the Effect of SiO_2-Graphene Oxide Hybrid as Inorganic Nanofiller on Corrosion Protection Properties of Epoxy Coatings, *Surf. Coat. Technol.*, 2017, **311**, p 282–294. https://doi.org/10.1016/j.surfcoat.2017.01.013
43. Y. Ye, D. Zhang, T. Liu et al., Superior Corrosion Resistance and Self-Healable Epoxy Coating Pigmented with Silanzied Trianiline-Intercalated Graphene, *Carbon*, 2019, **142**, p 164–176
44. Y. Ye, D. Zhang, J. Li et al., One-Step Synthesis of Superhydrophobic Polyhedral Oligomeric Silsesquioxane-Graphene Oxide and Its Application in Anti-Corrosion and Anti-Wear Fields, *Corros. Sci.*, 2019, **147**, p 9–21
45. HaoChen YuweiYe, Y. Zou and H. Zhao, Study on Self-Healing and Corrosion Resistance Behaviors of Functionalized Carbon Dot-Intercalated Graphene-Based Waterborne Epoxy Coating, *J. Mater. Sci. Technol.*, 2021, **67**, p 226–236
46. W. Sun, L. Wang, Wu. Tingting, Y. Pan and G. Liu, Synthesis of Low-Electrical-Conductivity Graphene/Pernigraniline Composites and Their Application in Corrosion Protection, *Carbon*, 2014, **79**, p 605–614. https://doi.org/10.1016/j.carbon.2014.08.021
47. J.H. Chu, L.B. Tong, M. Wen, Z.H. Jiang, K.S. Wang and H.J. Zhang, Graphene Oxide Film as a Protective Barrier for Mg Alloy: Worse or Better is Dependent on a Chemical Reduction Process, *Carbon*, 2019, **145**, p 389–400. https://doi.org/10.1016/j.carbon.2019.01.037

48. E.Y. Choi, T.H. Han, J. Hong, J.E. Kim, S.H. Lee and H.W. Kim, Noncovalent Functionalization of Graphene with End-Functional Polymers, *J Mater Chem.*, 2010, **20**, p 1907–1912
49. L.C. Tang, Y.J. Wan, D. Yan, Y.B. Pei, L. Zhao and Y.B. Li, The Effect of Graphene Dispersion on the Mechanical Properties of Graphene/Epoxy Composites, *Carbon*, 2013, **60**, p 16–27. https://doi.org/10.1016/j.carbon.2013.03.050
50. Hu. Xuebing, Yu. Yun, J. Zhou, Y. Wang, J. Liang, X. Zhang, Q. Chang and L. Song, The Improved Oil/Water Separation Performance of Graphene Oxide Modified Al_2O_3 Microfiltration Membrane, *J. Membr. Sci.*, 2015, **476**, p 200–204. https://doi.org/10.1016/j.memsci.2014.11.043
51. S. Yari and C. Dehghanian, Deposition and Characterization of Nanocrystalline and Amorphous Ni-W Coatings with Embedded Alumina Nanoparticles, *Ceram Int.*, 2013, **39**, p 7759–7765. https://doi.org/10.1016/j.ceramint.2013.03.033
52. W. Lv, D.M. Tang, Y.B. He, C.H. You, Z.Q. Shi, X.C. Chen, C.M. Chen, P.X. Hou, C. Liu and Q.H. Yang, Low Temperature Exfoliated Graphenes: Vacuum-Promoted Exfoliation and Electrochemical Energy Storage, *ACS Nano*, 2009, **3**, p 3730–3736. https://doi.org/10.1021/nn900933u
53. Y. Suzuki, S. Arai and M. Endo, Electrodeposition of Ni-P Alloy Multiwalled Carbon Nanotube Composite Films, *J. Electrochem. Soc.*, 2010, **159**, p 50–61
54. W. Sun, L. Wang, Wu. Tingting, Y. Pan and G. Liu, Synthesis of Low-Electrical-Conductivity Graphene/Pernigraniline Composites and Their Application in Corrosion Protection, *Carbon*, 2014, **79**, p 604–615. https://doi.org/10.1016/j.carbon.2014.08.021
55. C. Cui, A.T. Lim and J. Huang, A Cautionary Note on Graphene Anti-Corrosion Coatings, *Nat. Nanotechnol.*, 2017, **12**, p 834–835. https://doi.org/10.1038/nnano.2017.187
56. M.E. Uddin, T. Kuila, G.C. Nayak, N.H. Kim, B.C. Ku and J.H. Lee, Effects of Various Surfactants on the Dispersion Stability and Electrical Conductivity of Surface Modified Graphene, *J. Alloys Compd.*, 2013, **562**, p 134–142. https://doi.org/10.1016/j.jallcom.2013.01.127
57. R.S. Dey, S. Hajra, R.K. Sahu, C.R. Raj and M.K. Panigrahi, A Rapid Room Temperature Chemical Route for the Synthesis of Graphene: Metal-Mediated Reduction of Graphene Oxide, *Chem. Commun.*, 2012, **48**, p 1787–1789. https://doi.org/10.1039/c2cc16031e